1.11 In-flight ACIS Calibration Sources

1.11.1 Overview

The Observatory has two radioactive sources solely dedicated to ACIS calibration[10]. The first of these is the Internal Contamination Montior (ICM), located on the underside of the ACIS door. The flux from this tighly collimated source falls primarily on S2 Quad D and S3 Quads A-C. The purpose of the ICM is to allow an accurate measurement of line ratios immediately after launch. The post-launch ratio is then compared to the ratios determined during pre-flight testing. Discrepancies between the pre- and post-launch measurements would indicate the presence of contaminants on the ACIS detectors. Once the door is open, the ICM will not be visible again.

The second radioactive source is the External Calibration Source (ExtCalSrc), viewable by ACIS when the HRC-S is in the Observatory focus. The ExtCalSrc consists of three seperate sources that produce a number of Kα lines and illuminate the entire ACIS focal plane with near uniformity. The ExtCalSource will allow determination of chip gain and monitoring of other performance parameters during the entire lifetime of AXAF.

1.11.2 The Internal Contamination Monitor (ICM)

The Internal Contamination Monitor (ICM) is an ^{55}Fe source located on the inside of the ACIS door. Through electron capture, ^{55}Fe decays to ^{55}Mn through the channel: $^{55}_{26}\mathrm{Fe} + e^{-1} \rightarrow {}^{55}_{25}\mathrm{Mn}^{*} + \nu$. The excited Mn atom may then relax to the ground state through fluorescence of a photon of characteristic energy: $^{55}_{25}\mathrm{Mn}^{*} \rightarrow {}^{55}_{25}\mathrm{Mn} + \gamma_{\alpha}$, $\{ \gamma_{\alpha}$: K$_i$, L$_j$, M$_k$, $\cdots \}$. It is (mostly) the Mn K and L shell photons that are responsible for the observed spectrum.

The main purpose of the ICM is to monitor the potential accumulation of contaminants on the surface of the CCDs. The most probable contaminants are ice or hydrocarbons, and due their large absorption coefficients at the L-line energies ($\sim$ 640 eV), even a relatively thin layer of contamination would result in the attenuation of the L photons. At the K-line energies ($\sim$ 6 keV), however, the photons have a much larger attenuation length and would not be absorbed by the contaminants, much the way that high energy photons pass through the CCD gate structure and insulating layers. As the fluorescent yield of K to L photons from the radioactive source is constant, an increase of the K:L ratio would indicate the the build-up of contamination.

The initial Mn K and L fluorescence lines and additional lines they excite produce a

[10] A third source, attached to the HRMA cover, is intended for HRMA calibration and is not discussed here

rich spectrum that allows an accurate gain calculation. Thus, the ICM also has served as a gain calibrator during pre-launch calibration efforts and allowed a check of long-term gain stability of those CCDs illuminated by the ICM. Below, we carefully discuss the spectrum of the ICM and attempt to identify all the features present. We also measure the K:L ratio from three different measurements spanning over a year.

1.11.2.1 Spectrum

For the following analysis, we have used data from the TRW thermal vacuum tests (also referred to as AXAFTV) at TRW facilities during May-June, 1998. As the TV tests were primarily intended for a systems check of the entire spacecraft, ACIS was given limited time in telemetry format 2, the format used for acquiring science data. Instead, ICM data was collected in graded histogram mode. In this configuration the instrument finds and grades events, disregarding individual frames. Acceptable events (*ASCA* g02346) are written to a histogram, and after a specified number of frames, the histogram is telemetered.

The better response of the FI chip (relative to the BI chip) makes it the best choice for detailed studies of the ICM spectrum. Unless otherwise noted the data is from S2, quadrant D. At the same time, since most of the ICM flux falls on S3, we also discuss the data from the BI chip. In both cases, the data results from a total of 38,400 frames of normal integration (3.3 sec) data. Using a number of easily identified lines (see below), gains and offsets were calculated to convert energy units (ADU) to energy (keV). To facilitate the discussion, the spectral range is divided into three different energy bands, with only descriptive significance given to the names of each band.

Low Energy Band (0-1 keV): An examination of Figure 1.106 reveals a rich diversity of lines below 1 keV. There exists three main complexes of lines. The highest energy complex is clearly due to the three most common Ni L lines. The spectral resolution of the device does not allow separation of the individual lines. Instead, we have computed an average Ni L-line, using the expected intensities of the lines: α_1:α_1:β1 100:10:50. Table 1.75 lists the various low energy lines and computed average line energy for all the low energy features. The next complex, labeled the "L Complex" is centered around 0.67 keV. Although a gaussian nicely fits this feature, two problems exist with identifying it with a single emission line. First, the only line at this energy if F Kα_1 (677 eV) and no fluorine is present in the ICM. Second, the width of the best-fit gaussian to this features is twice as large as that measured for the width of the F Kα_1 during sub-assembly calibration. Thus, we conclude that this feature is a blend of at least two distinct lines, and most probably a combination of the expected Mn and Fe L lines. Referring to Table 1.75 and assuming equal contributions of the average Mn and Fe L lines, the identification of this feature as the "L Complex" becomes clear. Finally, there exists a complex centered around 0.55 keV. Due to the low count rate, a clear identification is not possible. At the same time, the tentative identification of the complex as a blend of O K$\alpha_{1,2}$ and Cr L seems rather reasonable.

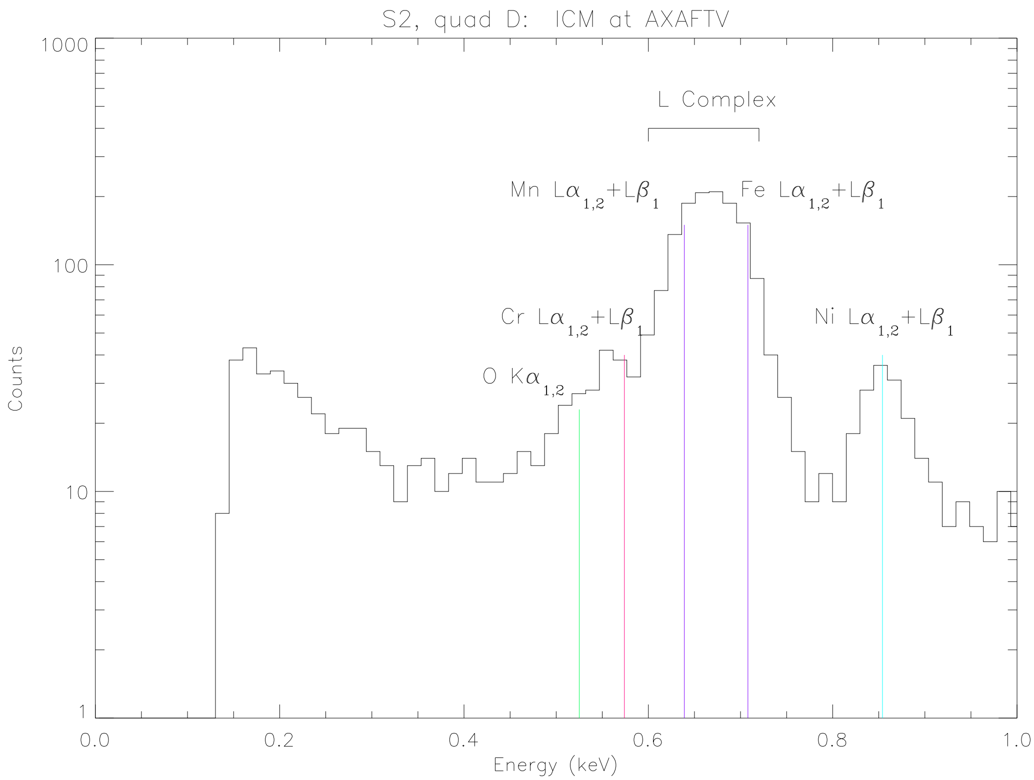

Figure 1.106: FI chip response to the ICM spectrum in the range 0-1 keV.

The poorer spectral resolution of the BI device and its slight non-linearity in gain blends the low-energy lines together and displaces the features with respect to their expected energy location as seen in Figure 1.107. Instead of the three complexes seen by the FI chip, there are only two visible in the BI chip. The Ni L line feature is still discernible, as is the Mn-Fe L complex, but it now contains the O Kα and Cr L lines. When a functional form is fit to the L complex to determine the K:L fluorescence yield, *what constitutes the L complex will differ between a BI and FI chip.* Thus, even after accounting for the different quantum efficiencies for the BI and FI chip, we expect K:L ratio as determined by the FI, will be higher than the K:L ratio measured by the BI chip.

Line	Energy (keV)	Line	Energy (keV)
O K$\alpha_{1,2}$	0.525		
Cr L$\alpha_{1,2}$	0.571	Fe L$\alpha_{1,2}$	0.704
Cr Lβ_1	0.581	Fe Lβ_1	0.717
<Cr L>	0.574	<Fe L>	0.708
Mn L$\alpha_{1,2}$	0.636	Ni L$\alpha_{1,2}$	0.849
Mn Lβ_1	0.647	Ni Lβ_1	0.866
<Mn L>	0.639	<Ni L>	0.854

Table 1.75: ICM lines in the 0-1 keV band

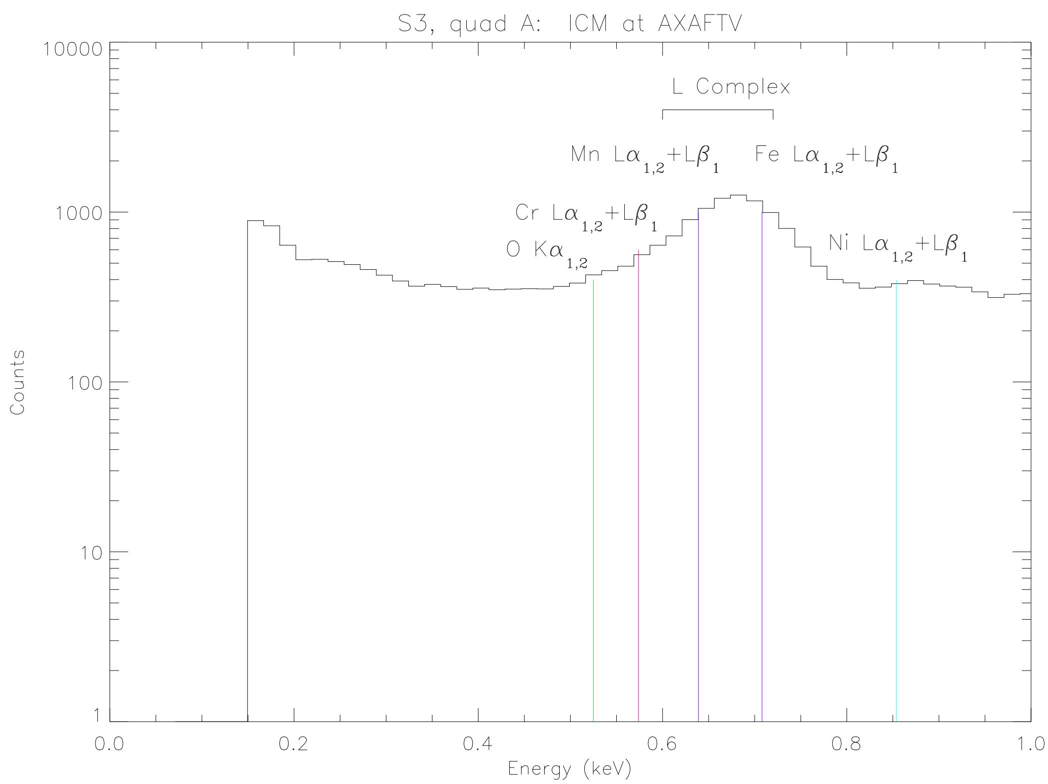

Figure 1.107: BI chip response to the ICM spectrum in the range 0-1 keV.

<u>Middle Energy Band (1-7 keV):</u> Figure 1.108 shows the FI response to the ICM source in the 1-7 keV band. In this energy range Mn emission lines are directly responsible for most of the spectral features. The two brightest lines are Mn K$\alpha_{1,2}$ and Mn Kβ_1. The corresponding escape features of these two lines are also present in the spectrum. The energies of the escape lines equal the emission line energy minus the energy of a Si K$\alpha_{1,2}$ fluorescence photon (1.74 keV). The Si K$\alpha_{1,2}$ fluorescence peak is also clearly visible. The relatively flat continuum at the $\sim$10 count level is the "shoulder" of both the Mn K$\alpha_{1,2}$ and Mn Kβ_1 lines that is due to the incomplete collection of the charge generated by the incident photons.

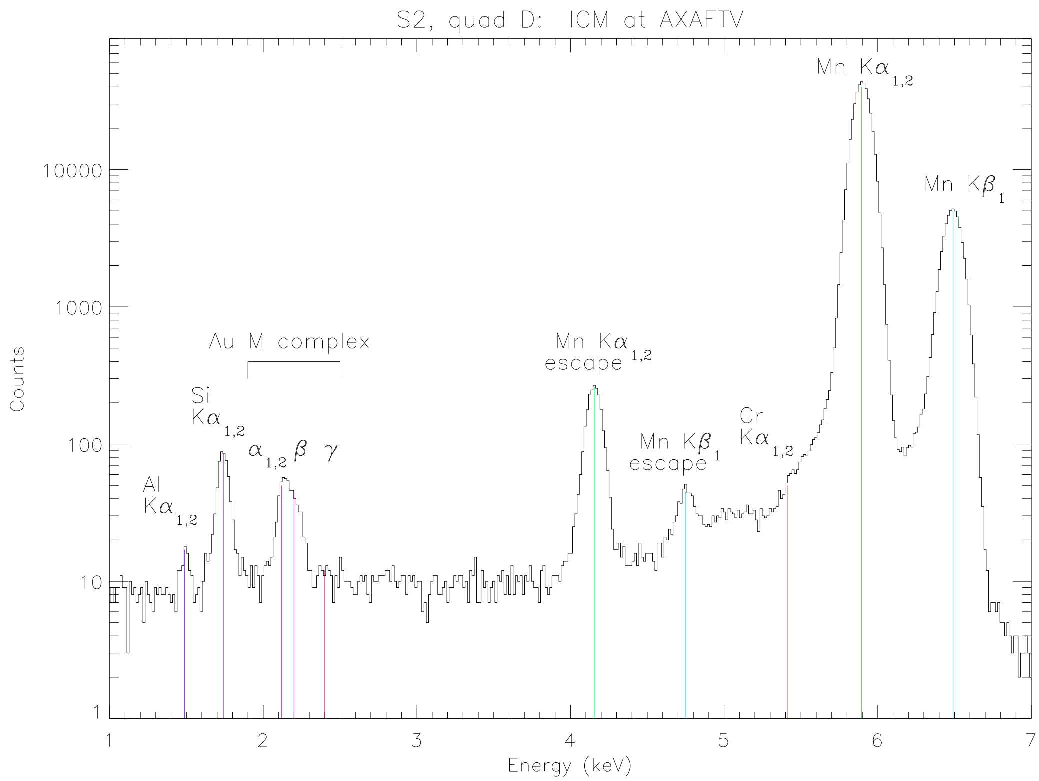

Figure 1.108: FI chip response to the ICM spectrum in the range 1-7 keV.

In addition to the the Mn lines, there is also weak evidence for a Cr K$\alpha_{1,2}$ line at the beginning of the Mn K$\alpha_{1,2}$ shoulder. Taken alone, the existence of the line seems marginal, but when coupled with detection of Cr L lines at lower energies, this identification becomes more secure. Finally, an Al K$\alpha_{1,2}$ line is clearly visible. Table 1.76 lists all the lines and energies for this band.

Line	Energy (keV)	Line	Energy (keV)
<Al K$\alpha_{1,2}$>	1.487	<Mn K$\alpha_{1,2}$> *esc*	4.155
<Si K$\alpha_{1,2}$>	1.740	Mn Kβ_1 *esc*	4.750
Au M$\alpha_{1,2}$	2.112	<Cr K$\alpha_{1,2}$>	5.411
Au Mβ	2.205	<Mn K$\alpha_{1,2}$>	5.895
Au Mγ	2.410	Mn Kβ_1	6.490

Table 1.76: ICM lines in the 1-7 keV band

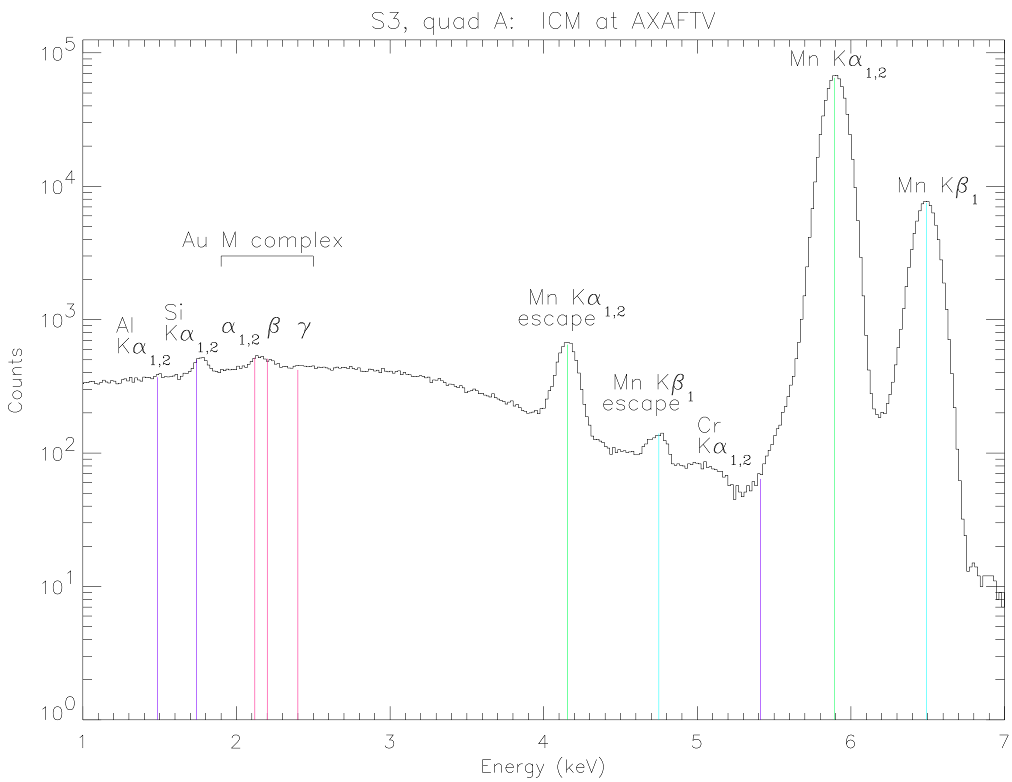

Figure 1.109: BI chip response to the ICM spectrum in the range 1-7 keV.

Figure 1.109 shows the BI response to the ICM source in the 1-7 keV band. In addition to the increased width of the spectral lines, the continuum level for the BI chip is much higher (a factor of ~20) and has a slow energy dependence. Due to the high continuum level, the Al K$\alpha_{1,2}$ line is not visible in the BI spectrum, and the Si K$\alpha_{1,2}$ line and Au M complex are just above the continuum level.

High Energy Band (7-15.5 keV): Figure 1.110 shows the FI response to the ICM source in the 7-15.5 keV band. Since this band begins at an energy above that of the highest Mn K emission line, we *a priori* expect 1) few events and 2) that those events will have an unusual origin. The rich spectral features arise from three distinct processes: pile-up, excitation by cosmic rays, and instrumental saturation. Pile-up results when charge from

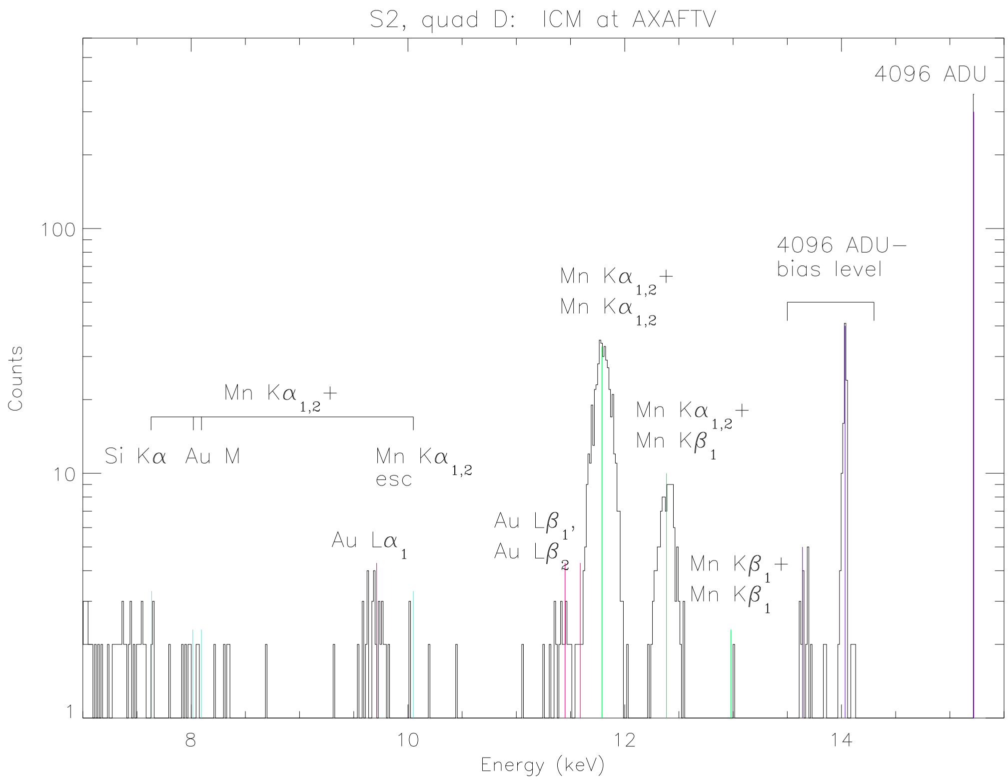

Figure 1.110: FI chip response to the ICM spectrum in the range 7-15.5 keV

two or more absorbed photons are collected in the same pixel during a single integration time. Since Mn K$\alpha_{1,2}$ is the most abundant line, it is not surprising that all but one of the pile-up "lines" involves the summation of a Mn K$\alpha_{1,2}$ with another line. Table 1.77 lists the seven most probable pile-up lines in this band and their energies. The counting statistics are too low to absolutely resolve all of the lines listed (Au M + Mn K$\alpha_{1,2}$, for example), but given a sufficiently long integration, their existence would be obvious. A completely different mechansim is responsible for the Au L lines. These lines arise not from the ICM source, but from cosmic rays that are absorbed by the Au covering of the frame store. The origin of these lines is confirmed by the existence of Au L and Au M lines in the spectrum of *all* CCDs, including ones that are not directly illuminated by the ICM.

This means that every spectrum will contain some level of Au M and Au L contamination. The highest energy features are due to the saturation of the digital chain. The spike at 15.22 keV corresponds to the highest analog-to-digital (ADU) value allowed (4096). The spikes at ~14.1 keV and ~13.7 keV correspond to 4096 ADU minus the bias level. The extremely narrow width of these line clearly indicates a non-emission origin. As the gain and bias level varies quadrant to quadrant, these features will occur at a range of energies. Table 1.77 also lists all the instrumental and cosmic-ray produced lines and energies.

Line	Energy (keV)	Line	Energy (keV)
Mn K$\alpha_{1,2}$ + Si K$\alpha_{1,2}$	7.635	Au Lβ_2	11.52
Mn K$\alpha_{1,2}$ + Au M$\alpha_{1,2}$	8.007	Mn K$\alpha_{1,2}$ + Mn K$\alpha_{1,2}$	11.79
Mn K$\alpha_{1,2}$ + Au Mβ	8.095	Mn K$\alpha_{1,2}$ + Mn Kβ_1	12.39
Au Lα_1	9.711	Mn Kβ_1 + Mn Kβ_1	12.98
Mn K$\alpha_{1,2}$ + Mn K$\alpha_{1,2}$ *esc*	10.05	4096 ADU - bias	13.6−14.2†
Au Lβ_1	11.44	4096 ADU	15.22†

†: these energies are dependent on the gain and bias levels and will vary from chip to chip

Table 1.77: ICM lines in the 7-15.5 keV band

Figure 1.111 shows the BI response to the ICM in the high energy band. In general, there is very little difference between the BI and FI spectra at the these energies. In addition to the discrete pile-up features, a flat continuum (few count level) extends from 7 keV up to highest pile-up line, a result of the summation of Mn K$\alpha_{1,2}$ photons with the low-energy tail from the Mn K lines. The energy response in the BI chips is higher than the FI chips ($\sim$ 18 keV versus $\sim$ 16 keV) due to the higher gain in the BI. The different gain and bias levels shifts the saturation features to higher energies than in the FI chip.

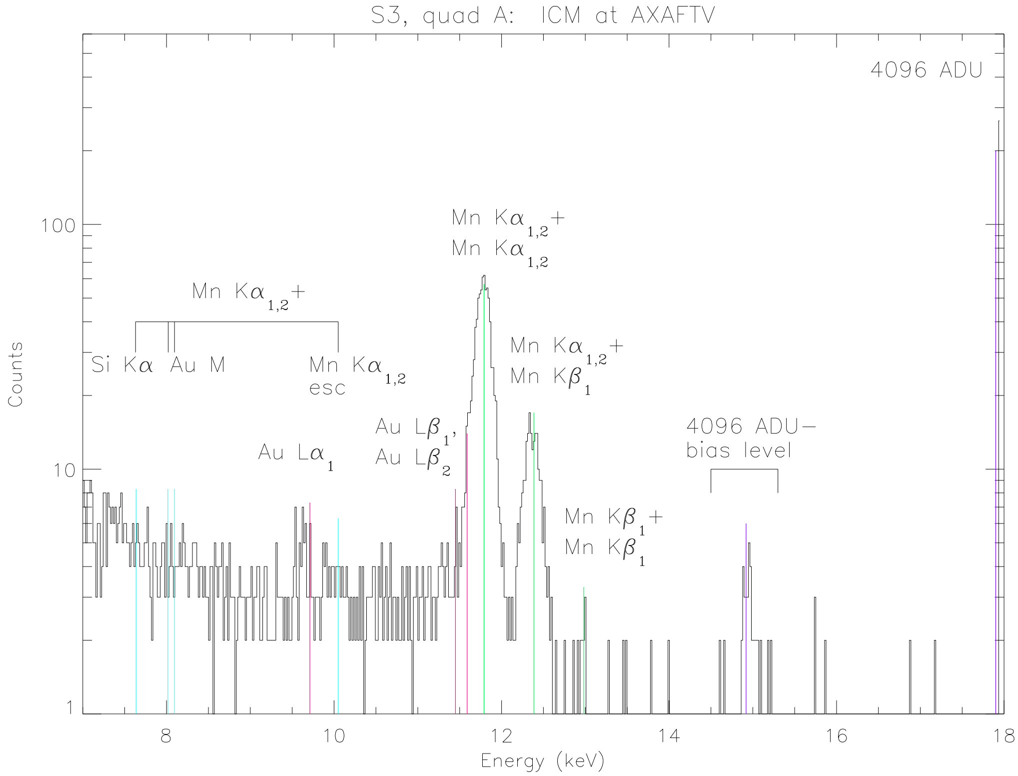

Figure 1.111: BI chip response to the ICM spectrum in the range 7-18 keV

1.11.2.2 Illumination Pattern

Before calculating the K:L ratio, it is necessary to check that the ICM source has not moved with respect to the focal plane. While the FI chips are flat, that is they show virtually no variations in QE or spectral response across their surface, the BI chips do have noticable spatial variations. If the area illuminated by the ICM changed from measurement to measuremnt, we might see variations in the K:L ratio. Figure 1.112 shows the illumination pattern of the ICM source on the focal plane. The map was made by selecting Mn K$\alpha_{1,2}$ events. Data was binned into 16 pixel$\times$16 pixel cells to smooth the Poisson fluctuations The chips were then normalized with respect to the maximum cell values. The spatial variations in the BI chip S3 are clearly visible as a general reduction in detection efficiency near the Quad A/Quad B boundary and the small fluctuations over Quads B & C. As long as the illumination pattern remains stable with time, however, these spatial variations will be normalized out of K:L ration calculation. Figure 1.113 shows the normalized contours of the Mn K$\alpha_{1,2}$ events from three different measurements: XRCF-I calibration from 1997

June, ISIM-TV measurements in 1998 January, and AXAF-TV measurements in 1998 May. Due to a lack of sufficient low temperature HST data, there are no intensity contours for S2 from AXAFTV. Nonetheless, it is clear that ICM position is stable with respect to the focal plane.

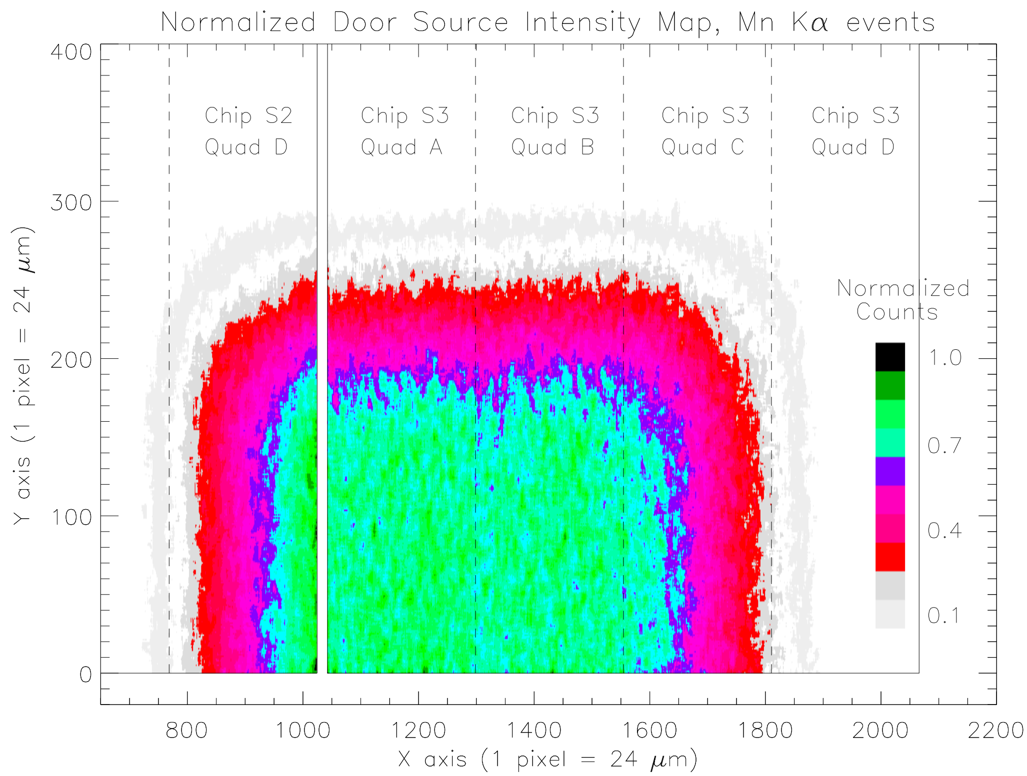

Figure 1.112: Illumination pattern of Mn K$\alpha_{1,2}$ events from the ICM as measured at XRCF-I

1.11.2.3 Mn K$\alpha_{1,2}$:L complex ratio

Code was written to ensure that the K:L would be calculated the same way for each additional measurement. For the FI chip S2 this involves fitting a gaussian model to the Mn K$\alpha_{1,2}$ line and a gaussian model to the combined Mn−Fe L feature. The K:L ratio is simply the ratio of the gaussian areas. For the BI chip S3 a gaussian was also fit to the Mn K$\alpha_{1,2}$ line. The poorer low energy spectral response required a more complicated function to accurately fit the L complex: a gaussian model with constant, linear and quadratic terms. The K:L ratio is still the ratio of the gaussian areas.

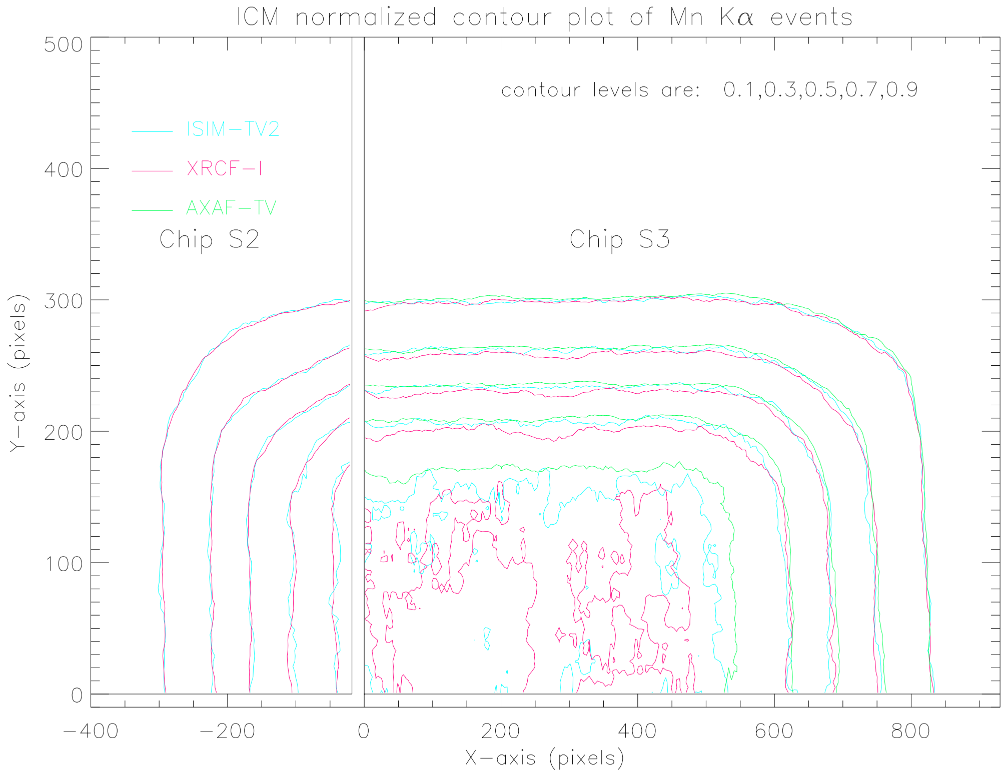

Figure 1.113: Contour map of ICM Mn $K\alpha_{1,2}$ events from three different measurements.

Table 1.78 presents the ratios for one S2 quadrant and three S3 quadrants from three different measurements. The quoted errors are 1 σ Poisson errors. For S2, the ratios are consistent within the errors, while for S3 the values show a larger than statistical variation. The mean and standard deviation of the nine points are 106.6 ± 5.16, clearly demonstrating that there is some unaccounted for systematic effect. If we disregard the highest and lowest values, the mean and standard deviation are 106.0 ± 2.30, closer to, but still higher than statistical fluctuations. The large difference between the BI and FI ratio is due to the BI's higher low energy quantum efficiency. Since we know the QE of both chips, the intrinsic K:L ratio can be calculated from both sets of data and compared as an additional check. We measure

$$R_{FI} = \frac{QE^{FI}_{MnK\alpha}}{QE^{FI}_{Lcomplex}} \times \frac{K}{L} \quad \& \quad R_{BI} = \frac{QE^{BI}_{MnK\alpha}}{QE^{BI}_{Lcomplex}} \times \frac{K}{L}$$

where R_i is the K:L ratio for the BI or FI chip, QE^i_j is the quantum efficiency for the i^{th} chip at energy j, and $\frac{K}{L}$ is the intrinsic Mn $K\alpha_{1,2}$ to Mn−Fe L complex ratio. Since the L complex is a blend of lines, we approximate the low energy QE as the average of the mean QE's at Mn L and Fe L, which themselves are weighted averages of the various L lines. Table 1.79 lists the appropriate quantum efficiencies, the measured ratios, and the calculated intrinsic ratios. While the ratios are much closer to agreeing, there is still a ~15% discrepancy. If we then consider that BI $\frac{K}{L}$ value should be higher, due to the addition of the O Kα and Cr L flux in the L complex (see Section 2 for details), the discrepancy becomes larger. At the same time, however, our approximation laden method clearly over-simplifies the situation. Our averaging of discrete QE values over a wide energy pass band introduces errors into the low energy QE. Also, our simplistic gaussian + background model of the L complex cannot account for the complicated spectral redistribution function of the BI. A reliable, exact comparison demands that an accurately modeled ICM source spectrum be folded through both the BI and FI response matrices.

		S2		S3	
Location	Date	Quad D	Quad A	Quad B	Quad C
XRCF-I	01Jun97	293.9 ± 5.82	109.1 ± 1.04	103.8 ± 0.97	105.7 ± 1.20
ISIM-TV2	16Jan98	278.8 ± 9.65	104.3 ± 1.74	108.9 ± 1.85	117.8 ± 2.55
AXAF-TV	16May98	287.3 ± 3.81	106.5 ± 0.68	99.33 ± 0.62	103.6 ± 0.80

Table 1.78: Mn K$\alpha_{1,2}$:Mn–Fe L complex ratios

	Quantum Efficiency		Measured	Intrinsic
Chip	<0.674 keV >	5.895 keV	Ratio (R)	Ratio ($\frac{K}{L}$)
FI	0.365	0.910	287	115
BI	0.952	0.747	106	135

Table 1.79: The intrinsic strength of the Mn K$\alpha_{1,2}$ line to the L complex

1.11.3 The External Calibration Source (ExtCalSrc)

The External Calibration Source (hereafter abbreviated ExtCalSrc) consists of three separate radioactive sources held in a common holder. While all three sources contain ^{55}Fe, they each predominately produce lines of different energies. Two widely collimated sources use the Mn Kα and Mn Kβ photons to fluoresce either Ti or Al and excite those characteristic K emission lines. The third source does not fluoresce another metal and mainly emits only Mn K and L photons. Some of the Mn photons pass through the Al and Ti sources without being absorbed, so these sources also produces Mn K and L lines. The ExtCalSrc illuminates the ACIS focal plane only when the HRC-S instrument is in the telescope focus position. The various emission lines produced by the ExtCalSrc will allow an accurate gain measurement for each node of each ACIS CCD. With sufficiently long integrations, the ratio of the Mn Kα flux to the Mn L-Fe L flux can be measured and used to monitor the potential accumulation of contaminants on ACIS (see Section 1.11.2 for the details of this technique). Below, we discuss the spectrum of the ExtCalSrc, the expected count rate in the Al, Ti and Mn Kα lines, and the spatial distribution of the flux.

1.11.3.1 Spectrum

Figure 1.114 shows the spectrum of the ExtCalSrc from S2. The data consists of a 9.2 ks exposure of HST data. After accounting for the different gains of each quadrant, the data from each output was summed together to increase the signal. The most obvious features are the easily discernible Kα and Kβ lines needed for accurate gain measurements. A number of other, well-understood features are present and are discussed below. The lowest

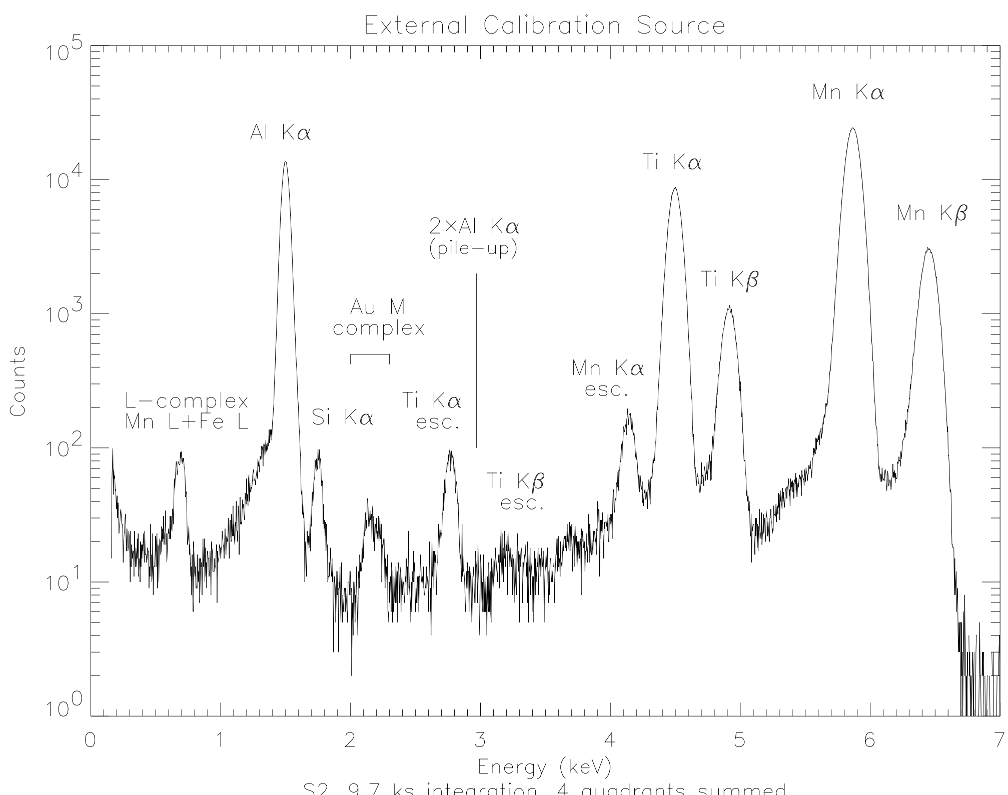

Figure 1.114: ExtCalSrc spectrum (0-7 keV) on S2 from a 4 $\times$ 9.2 ks integration

energy complex is a blend of Mn Lα, Mn Lβ, Fe Lα, and Fe Lβ lines. The CCD resolution does not allow differentiation between the Mn and Fe lines (ΔE $\approx$ 60 eV apart) and they appear as a single line. See Section 1.11.2.1 for a detailed discussion on the characteristics of the L complex. The next feature is the Al Kα emission line with its very well defined low-energy shoulder. Right above that is the Si Kα fluorescence line. These photons are produced when an incident photon of higher energy interacts inside the CCD and produces a Si Kα photon. If the photon travels far enough from the interaction sight in the proper direction, it can be detected. Regardless on whether the Si Kα photon is detected, if it travels sufficiently far from the initial absorption site, the charge deposited at that site will equal the energy of the incident photon - 1740 eV (Si Kα energy). These feature are the escape features of an emission line. Both the Mn and Ti Kα escape features are clearly present and nearly gaussian. Ti Kβ escape is also present, but with fewer events. Mn Kβ escape is also present, but is hidden by the Ti Kβ line. The well-defined, but irregularly shaped feature around 2.2 keV is the Au M complex, a number of closely spaced Au M lines. The lines are produced by fluorescence of the gold coating on the outer surface of the radioactive sources. Finally, we have indicated where the pile-up line of Al Kα would occur. There is a hint of counts above the background at the appropriate energy, but low statistics prevents a firm detection. Certainly, pile-up is always present at some level, but the incidence for the ExtCalSrc is small and will only decrease as the ^{55}Fe decays. For a discussion of the features present above 7 keV, we again refer the reader to detailed discussion in Section 1.11.2.1. Table 1.80 lists the lines and energies of all the labeled features in Figure 1.114.

Line	Energy (keV)	Line	Energy (keV)
Mn L$\alpha_{1,2}$	0.636	<Ti K$\alpha_{1,2}$> *esc*	2.768
Mn Lβ_1	0.647	2 $\times$ <Al K$\alpha_{1,2}$>	2.974
Fe L$\alpha_{1,2}$	0.704	Ti Kβ_1 *esc*	3.191
Fe Lβ_1	0.717	<Mn K$\alpha_{1,2}$> *esc*	4.155
<Al K$\alpha_{1,2}$>	1.487	<Ti K$\alpha_{1,2}$>	4.508
<Si K$\alpha_{1,2}$>	1.740	Mn Kβ_1 *esc*	4.750
Au M$\alpha_{1,2}$	2.112	Ti Kβ_1	4.931
Au Mβ	2.20	<Mn K$\alpha_{1,2}$>	5.895
Au Mγ	2.410	Mn Kβ_1	6.490

Table 1.80: ExtCalSrc lines in the 0-7 keV band

1.11.3.2 Count Rate

It is important to accurately measure the count rate of the largest emission features of the ExtCalSrc, mainly the Al, Ti, and Mn Kα lines for two reasons. First, the accuracy of the gain calculations needed for continual ACIS calibration depends on how well the line centers are measured, which in turn depends on the number of counts in the peak. With an accurate count rate in hand, we can calculate the time needed to collect the counts for the desired level of gain accuracy. Second, knowing the count rates will allow adjustment of the spatial windows to avoid saturating telemetry and to maximize the amount of calibraiton data.

The ExtCalSrc was carefully measured on 23 October 1997 during the first ISIM thermal vaccuum testing (ISIM-TV1). Because both spatial and spectal information were desired and full-frame data on six chips would have saturated telemetry, we acquired a mininum of $\sim$1500 HST frames for each chip. Gaussian lines were then fit to the Kα peaks, and the count rates simply equal the gaussian area/integration time. Table 1.81 present the count rates and errors, where the errors are the 1 σ Poisson noise.

Chip	Mn Kα (cnt s^{-1} chip^{-1})	Ti Kα (cnt s^{-1} chip^{-1})	Al Kα (cnt s^{-1} chip^{-1})
I0	89.69 $\pm$ 0.13	25.65 $\pm$ 0.07	25.86 $\pm$ 0.07
I1	89.44 $\pm$ 0.13	26.02 $\pm$ 0.07	25.89 $\pm$ 0.07
I2	90.57 $\pm$ 0.19	26.93 $\pm$ 0.10	26.48 $\pm$ 0.10
I3	89.58 $\pm$ 0.13	27.29 $\pm$ 0.07	26.38 $\pm$ 0.07
S0	87.34 $\pm$ 0.13	24.54 $\pm$ 0.07	25.55 $\pm$ 0.07
S2	92.08 $\pm$ 0.13	28.10 $\pm$ 0.07	27.14 $\pm$ 0.07
S4	89.48 $\pm$ 0.13	28.77 $\pm$ 0.07	26.36 $\pm$ 0.07
S5	87.61 $\pm$ 0.13	28.40 $\pm$ 0.07	24.98 $\pm$ 0.07
S1	59.12 $\pm$ 0.11	22.14 $\pm$ 0.06	29.46 $\pm$ 0.07
S3	72.98 $\pm$ 0.08	27.45 $\pm$ 0.05	31.04 $\pm$ 0.05

Table 1.81: Observed Counting Rate from the External Cal Source on 23 October 1997

Two general facts are immediate noticable. First, the ratio of Mn Kα:Ti Kα:Al Kα is $\sim$4:1:1 for the FI chips and $\sim$2:1:1 for the BI chips. The large difference in the ratio and the differences in the actual count rates are due to the general variations in quantum efficiences between BI and FI chips. Second, the fluctuation in count rate between FI chips is much larger than the stastical errors. In some cases this is at least partially attributable to slightly different QEs, but the largest contributor to this effect is the physical distribution of incident photons (see the section below on spatial uniformities).

The observed flux from the ExtCalSrc will exponentially decrease with time as the source ^{55}Fe radioactively decays. Using the published half-life value $T_{1/2} = 2.73$ yr, we have calculated what the count rates for the three primary lines will be during the early days of AXAF's orbital operation. Table 1.82 lists the count rates for a typical FI chip and both BI chips.

Chip	Mn Kα (cnt s^{-1} chip^{-1})	Ti Kα (cnt s^{-1} chip^{-1})	Al Kα (cnt s^{-1} chip^{-1})
<FI>	62.1	18.7	18.1
S1	41.0	15.4	20.5
S3	50.7	19.1	21.6

Table 1.82: Predicted Count Rate for 01 April 1999

1.11.3.3 Spatial Distribution

While the spatial distribtuion of ExtCalSrc flux does not directly influence the gain calculation, it is intimately tied to the detected count rate of the Kα lines. Two types of variation are observed. First, for a given source, there will be a certain pattern expected from its collimation beam and a reduction of intensity as the distance from the source axis increases. Second, since the photons for each flavor of Kα lines come from a seperate source, we expect that intensity patterns will vary source to source. The housing for the ExtCalSrc contains locations for four individual sources (only three are occupied). Looking down on the focal plane such that S0 is in the lower left and I1 in the upper right (see Figures below), the Al source is in the upper left, the Ti source is in the upper right, and the Mn source is in lower left. Figures 1.115, 1.116, & 1.117 contain the intensity maps for each Kα line. To account for chip-to-chip differences in quantum efficiency, all the chips have been normalized to the QE of S2 at each energy. For example, if S0 is only 90% as efficient as S2 at Al Kα, the observed Al Kα intensity for S0 is multiplied by 1.0/0.9. Each 1024$\times$1024 CCD image was binned into a 64 $\times$ 64 array (16 pixels$\times$16 pixels/cell). For the typical 4800 sec exposures taken during ISIM-TV1, the total counts in a single cell is approximately equal to the count rates in Table 1.81. Since the Poisson noise was rather large (19%, 17%, and 10% for Al, Ti, and Mn) the images were smoothed with a 5$\times$5 box car function to reduce 1 σ statistical fluctuations to the $\sim$5% level. Finally, the map was normalized with respect to the mean intensity of S2 (i.e. the mean intensity of S2 is unity for all the maps).

The most obvious of the macroscopic features is the patchy nature of the maps that results from Poisson fluctuations. The BI chips also contain significant banded structure along the quadrant boundaries and the top (row 1024) of the chip. This structure results from using a global value for the quantum efficiency, rather than accounting for the measured spatial variations in QE. This effect is most notable in chip S1 at Ti and Mn[11]. Finally, the intensity distribution is discernable. For example, at Mn chips S4 and S5 have less flux, consistent with the placement of the bare ^{55}Fe source in the lower left of the ExtCalSrc holder. The Ti intensity dramatically dereases at the outer edge of S0, while the Al intensity drops dramatically at the egde of S5. Both of these structures also agree with placement of the Ti source in upper right holder position (furthest from S0) and the Al source in the upper left holder position (futherest from S5).

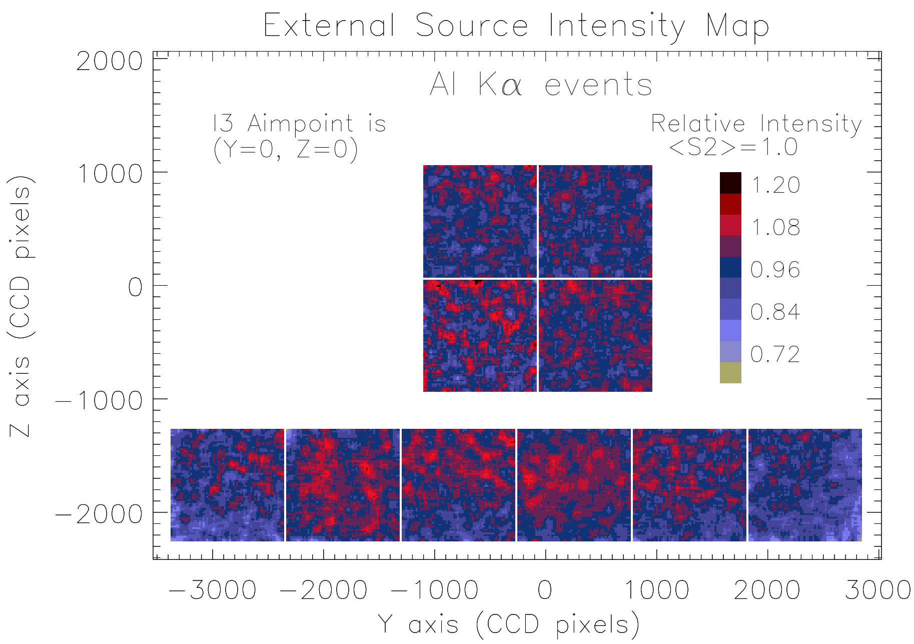

Figure 1.115: Relative intensity map of ExtCalSrc Al Kα. Quantum efficiencies have been normalized with respect to S2. Intensities were then normalized with resepct to S2.

[11]In the future, a spatially dependent QE map will be used to correct for the large QE variations across the BI chips. This measure will eliminate the banding and related structure in these intensity maps.

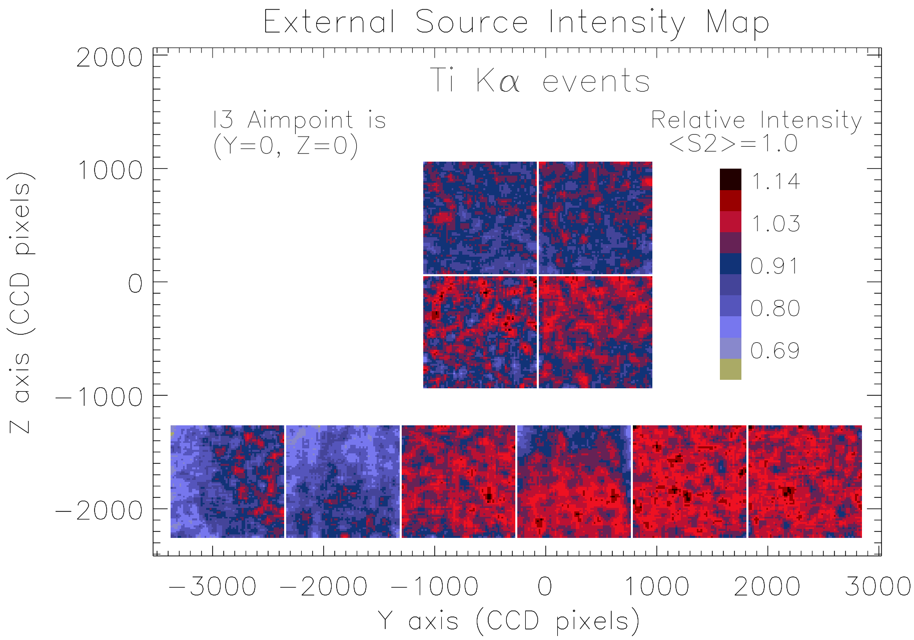

Figure 1.116: Relative intensity map of ExtCalSrc Ti Kα. Quantum efficiencies have been normalized with respect to S2. Intensities were then normalized with resepct to S2.

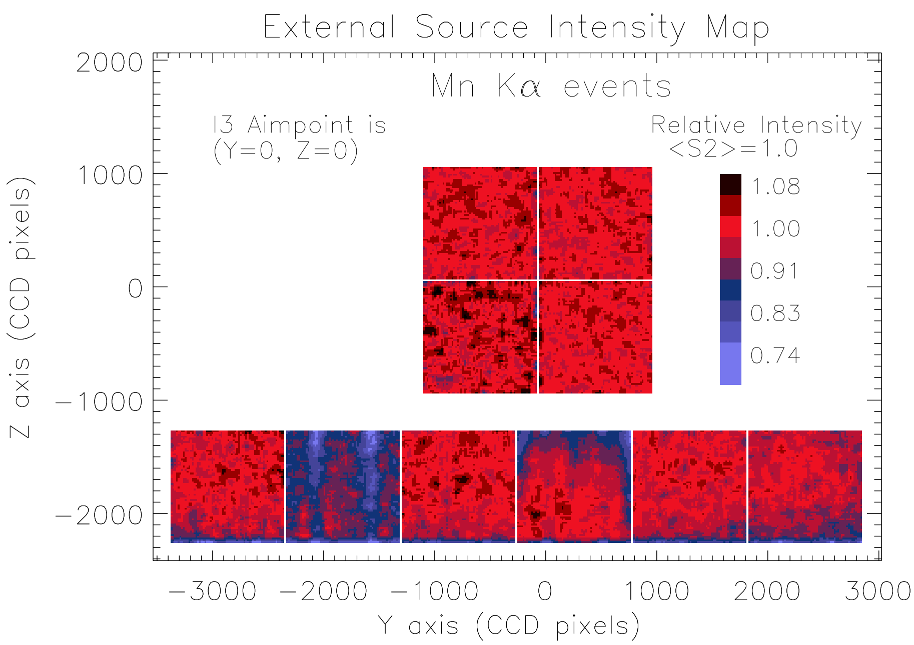

Figure 1.117: Relative intensity map of ExtCalSrc Mn Kα. Quantum efficiencies have been normalized with respect to S2. Intensities were then normalized with resepct to S2.